Quantifying Contribution of Atmospheric Circulation to Precipitation Variability and Changes in the U.S. Great Plains and Southwest Using Self Organizing Map – Analogue

Yizhou Zhuang[1], Rong Fu[1]

[1]Department of Atmospheric and Oceanic Sciences, University of California, Los Angeles, CA 90095, USA

Correspondence to: Yizhou Zhuang (zhuangyz@atmos.ucla.edu)

Abstract. The Great Plains and Southwest regions of the U.S. are highly vulnerable to precipitation-related climate disasters such as droughts and floods. In this study, we propose a self-organizing map–analogue (SOMA) approach to empirically quantify the contribution of atmospheric circulation (mid-tropospheric geopotential and column moisture transport) to the regional precipitation anomalies, variability, and multi-decadal changes. Our results indicate that atmospheric circulation contributes significantly to short-term precipitation variability, accounting for 54-61% of the total variance and 62-68% of the amplitude of the mean precipitation anomalies in these regions, though these contributions vary significantly across seasons. The remaining variance is largely influenced by thermodynamically driven factors. As indicated in previous research, Pacific Decadal Oscillation (PDO) is one of the major climate modes influencing the long-term multi-decadal variation of precipitation. By contrasting three multi-decadal periods (1950-1976, 1977-1998, 1999-2021) with shifting PDO phases and linking the phase shift to circulation SOM nodes, we found that circulation changes contribute considerably to the multi-decadal changes of precipitation anomaly in terms of the mean and probability of dry and wet extremes, especially for the Southern GP and Southwest. However, these circulation-induced changes are not totally related to the PDO phase shift (mostly less than half), atmospheric internal variability or anthropogenically induced changes in circulation can also be potential contributors. Our approach improves upon flow analogue and SOM-based methods and provides insights into the contribution of atmospheric circulation to regional precipitation anomalies and variability.

1 Introduction

The United States Great Plains (GP) and Southwest (SW) are central to national and global agricultural production (Elias et al., 2016; Parton et al., 2015). As the drier half of the continental United States (CONUS) with high variability of precipitation, the GP and SW rely on irrigation much more heavily than the eastern states and they are known to be susceptible to climate disasters such as extreme droughts, wildfires, storms, and flooding, which are all listed among the top billion-dollar weather and climate disasters (NCEI, 2023). Understanding the driving factors and mechanisms for the occurrence of precipitation anomalies is crucial for the evaluation and improvement of current prediction systems as well as water resource management.

Past studies have reported various mechanisms that link to the precipitation variability in North America, including anthropogenic forcings (Kirchmeier-Young and Zhang, 2020), internal atmospheric variabilities (Mckinnon and

Deser, 2021), El Nino/Southern Oscillation (ENSO) (Hu and Huang, 2009), Pacific Decadal Oscillation (PDO) (Lehner et al., 2018), Pacific-North America (PNA) (Zhuang et al., 2021a), Atlantic sea surface temperature (Hu and Feng, 2008), each of which can contribute differently for different locations, time scales, seasons, or even individual events. These internal variabilities and large-scale remote forcings influence the local precipitation either through affecting the atmospheric circulation conditions above (dynamics) or some local and remote land surface feedbacks (thermodynamics), both of which control the vertical air motion and moisture support that finally lead to precipitation. Another critical scientific question is to what extent can anthropogenic warming affect precipitation and hydroclimate variability and their long-term changes. Modern coupled climate model simulation has been one of the most important tools for these attribution studies. Such model simulation can reproduce the observed trends of the hydroclimate through contrasting simulations with and without anthropogenic forcings. It is basically a common consensus that the temperature increase trend will continue and exacerbate the future drought condition through enhancing evaporative demand. Yet, climate models have struggled producing reliable precipitation simulation and predictions, and multiple models participated in the CMIP5 and CMIP6 projects show a wide range of inconsistency for future projection. Many recent studies have argued that the long-term precipitation changes in these regions, at least from the mid-20th century until now, is primarily driven by PDO induced atmospheric teleconnection to North America, instead of anthropogenic warming, as evident by the relatively dry periods with negative PDO phase (1940s-1970s and 1999 onwards) when many of the major drought events occurred (Hoerling et al., 2014; Seager et al., 2014; Mankin et al., 2021), and a relatively wet period with positive phase (1980s-1990s). Yet, it is not clear quantitatively how much these long-term changes of precipitation can be explained by the atmospheric circulation variability or the PDO related circulation variability.

The self-organizing map (SOM) or Kohonen Map (Kohonen, 1990), an unsupervised neural network-based clustering method, has long been demonstrated as an effective and powerful tool to study dynamics or atmospheric circulation patterns related to precipitation variability, drought, or other atmospheric/oceanic phenomena (Liu and Weisberg, 2011; Zhuang et al., 2020). Different from other clustering methods, such as K-means and hierarchical clustering, SOM has the advantage of sorting samples into types (SOM nodes) connected to each other in a "map" that preserves the topological structure of the data, so similar types are close to each other. Based on SOM, Cassano et al. (2007) proposed a quantitative partitioning method (refer to as "C2007" hereafter) to determine the dynamic and thermodynamic contributions to anomalies or trends of surface parameters such as precipitation. The idea is that the total anomaly of a surface parameter (e.g., precipitation P') can be decomposed as the sum of a dynamic component (P'_{dyn}) controlled by the mean frequency change of SOM nodes, a thermodynamic component (P'_{the}) related to the mean state change of the surface parameter for the same SOM node, and an interaction term (P'_{int}) related to both. Detailed descriptions of this method can be referred to Cassano et al. (2007) and Horton et al. (2015). However, this partitioning method assumes that the P'_{dyn} at the time scale of individual sample (e.g., daily) stays the same for circulation patterns classified to the same SOM node. This underlying assumption leads to the result that the determination of P'_{dyn} could be sensitive to the choice of SOM node number. An additional inconvenience related to this method is that the SOM analysis is often conducted in certain seasons as the circulation–surface anomaly relationship could vary in different seasons.

70   Flow analogue (Jezequel et al., 2018; Yiou et al., 2007) or dynamic adjustment (Deser et al., 2016; Lehner et al., 2018) is another widely used method (refer to as analogue hereafter) to determine the dynamic contribution. For a certain day (or other time scales), different from the C2007 method, the analogue method searches for a limited number of days (analogue days) with circulation patterns most similar to that of the target day, instead of days assigned to the same SOM node in C2007; it then combines the surface anomaly of these analogue days to form a final analogue

75   anomaly or dynamic component (P'_{dyn}), and the residual from the observed anomaly can be defined as the thermodynamic component (P'_{the}). Detailed steps and variants of the analogue method can be found in the literature (Zhuang et al., 2021b). The analogue theoretically better estimate the dynamic contribution by utilizing circulation patterns from the analogue days and accounting for their subtle difference.

In this study, we proposed a modified approach to quantify the multivariate circulation contribution to P' in terms of

80   its daily variability and amplitude of anomaly, combining the advantages of both SOM and constructed analogue methods. We further use this approach to quantify the contribution of overall circulation changes and potentially PDO-related circulation changes to the long-term multidecadal changes of P'.

The datasets and methods used in this study are described in section 2. All the main results, including the SOM inferred relationship between large-scale atmospheric circulation and precipitation and SOM – analogue based quantification

85   of circulation contributions to precipitation anomalies, their variability and long-term changes, are presented in section 3. Section 4 summarizes the main conclusions of this study and also gives a brief discussion about the implication of this study, limitation of our methodology and results, and possible future research directions.

2 Data and Method

2.1 Data

90   In previous studies related to SOM and analogue, large-scale circulation is generally represented by mean sea level pressure (SLP) or geopotential height at 500 hPa (Z500). Here, we choose Z500 over SLP as experiments show analogues derived from Z500 show more similar synoptic variability with observed surface anomalies and smaller residuals than analogues derived from SLP (Zhuang et al., 2021b). On the other hand, impacts of anomalous atmospheric moisture transport represented by vertically integrated vapor transport (IVT) on precipitation variability

95   and drought are also suggested in the literature (Zhuang et al., 2020; Pu et al., 2016; Swales et al., 2016). The 3-hourly Z500 and IVT data at 1°×1° resolution are obtained from the fifth generation ECMWF atmospheric reanalysis of the global climate (ERA5) (Hersbach et al., 2020). We use their daily averages for all months from 1950 to 2021 over the CONUS area (130°-70°W, 25°-55°N) as input for later analyses. To account for the thermal expansion of the warming atmosphere, we subtract the daily global area-weighted mean Z500 from the daily Z500 data at each grid point before

100   further processing (Christidis and Stott, 2015; Siler et al., 2019; Zhuang et al., 2021b). A simple pentad moving average filter is applied to reduce high-frequency synoptic noise. Daily standardized anomaly (Z500′ and IVT′) is calculated relative to the 1950-1999 climatology. We follow the running mean approach used in Zhuang et al. (2020) to calculate a smooth daily climatological mean and standard deviation.

For precipitation, the Climate Prediction Center (CPC) global unified gauge-based analysis of daily precipitation (P)
is used. This dataset is at 0.25°×0.25° resolution and covers the period from 1948 to the present. In this study, we
mainly focus on three regions, including the Southern GP (SGP; 105°-92°W, 26°-38°N), the Northern GP (NGP;
105°-92°W, 38°-49°N), and the Southwestern US (SW; 114°-105°W, 31°-42°N). Therefore, area-weighted mean
precipitation is calculated over these three regions. A pentad moving average filter is also applied to precipitation
similar to the circulation data. The precipitation anomaly (P') is calculated relative to 1950-1999 climatology using
the same approach stated above for circulation, but without the standardization process as precipitation generally
follows a gamma distribution rather than Gaussian distribution.

Besides circulation and precipitation, other data used in this study including ERA5 2-m dewpoint temperature (D2),
700hPa temperature (T700) data, and convective available potential energy (CAPE), as well as the monthly Pacific
Decadal Oscillation (PDO) index provided by the National Center for Environmental Information (NCEI). The D2
and T700 data are used to calculate the convective inhibition (CIN) index (CINi = D2 – T700) (Myoung and Nielsen-
Gammon, 2010) to represent the lower atmospheric instability; ERA5 also provides CIN data but it is not always
available around the year due to its original definition from the parcel buoyancy model. Both CAPE and CINi data
are processed the same way as circulation data to acquire their standardized anomalies (CAPE′ and CINi′) for further
analyses. The PDO index is one of the most important Pacific climate variability and often described as an El Nino-
like pattern but with long-term persistence up to several decades (Zhang et al., 1997). The NCEI monthly PDO index
is calculated based on the NOAA extended reconstruction of sea surface temperature version 5 (ERSSTv5). Our whole
analysis period 1950-2021 can be divided into three periods, each with different PDO phase from its previous one,
including P1: 1950-1976 (negative), P2: 1977-1998 (positive), and P3: 1999-2021 (negative). Long-term change of
precipitation in terms of its mean or probability of extremes for our following analysis (section 3.3) is defined as the
difference between two adjacent periods (P2 – P1 and P3 – P2).

2.2 Method

2.2.1 Multivariate SOM

In this study, large-scale atmospheric circulation condition is jointly represented by Z500′ and IVT′, as both of them
have been demonstrated to be important for the precipitation variability over North America. The data matrices of
these two variables are concatenated along the spatial dimension, so the input data matrix has a size of ($2 \times N_{lon} \times N_{lat}$,
N_t). Specifically for this study, the input size is ($2 \times 61 \times 31$, 365×72).

To speed up the SOM training process, we employ a principal component analysis (PCA) preprocessing technique
(Zhuang et al., 2020). PCA or Empirical Orthogonal Functions (EOF) is a widely used approach for data dimension
reduction or extracting spatial modes of variability (Reusch et al., 2005). Here, PCA is used to decompose the high
dimensional circulation data (two variables and thousands of grid points) into the matrix multiplication product of
some low dimensional principal components (PCs) and their corresponding loading vectors (modes). By only retaining
the top PCs and modes that explain the majority of the variance in the original data, the PCs can be used as reduced-
size input data for SOM. Specifically in this study, we retain the top 26 PCs which explain 90.6% and 77.4% of the
variance in Z500′ and IVT′, respectively, or 87.3% of their combined variance.

140   Determination of SOM node number and evaluation of the trained SOM quality are often complicated issues. Too few SOM nodes could lead to an underrepresentation of samples, while too many nodes likely will result in redundancy and create difficulties for analysis and visual interpretation. In this study, we have tested multiple SOM schemes with various node numbers up to 200. Three metrics are calculated for the trained SOM of each scheme to assess the SOM quality, including the quantization error (QE), topographic error (TE), and combined error (CE). QE represents the

145   average Euclidean distance between each data vector and the SOM node it is assigned to, or the so-called best matching unit (BMU). TE is the proportion of all input data vectors which have first and second BMUs that are not adjacent to each other in the SOM map. CE is a metric that combines the concepts of both QE and TE and was defined by Kaski & Lagus (1996).

SOM training and error metric calculation are performed using the Matlab SOM Toolbox (Vatanen et al., 2015).

150   Training length is fixed at 100 epochs (50 for rough training and 50 for fine-tuning) for all schemes. Additional experiments show that increasing training length can reduce QE, but the improvement is very marginal after around 100 epochs (not shown). In the SOM Toolbox, after inputting a desired node number, the SOM map shape is automatically determined. After training SOMs for all schemes with various node numbers and calculating their quality metrics, the result in Fig. 1 shows that overall, QE decreases with node number as more nodes mean more

155   detailed classification of circulation patterns and thus are more representative of individual samples; TE increases with node number as a more complex network often leads to a larger topographic structure; CE, which combined the concepts of both quantization and topographic errors, decreases with node number first when the number is relatively small and then exhibits larger fluctuation than QE and TE. A 7×4 SOM scheme is chosen for our following analysis as this scheme has a relatively smaller node number that facilitates the visualization and analysis of the results and

160   also has a lower CE compared to schemes with similar node numbers.

2.2.2 Empirical quantification dynamic contribution: SOM-Analogue (SOMA) Method

As stated in the introduction section, the C2007 dynamic/thermodynamic partition method assumes the mean P' of all days with the same BMU node as its dynamic component, i.e., P'_{dyn}. However, this approach can underestimate of variability in true P'_{dyn}, especially when the node number issmall and the circulation pattern of a BMU is less

165   representative of the assigned samples. On the other hand, the flow analogue method (e.g., Yiou et al. 2007; Zhuang et al. 2021), estimates P'_{dyn} for a given day by identifying historical days with similar atmospheric circulation condition (analogue days) and combining the P' information from these selected analogue days. Specifically, the flow analogue method employed by Zhuang et al. (2021) follows three main steps. First, for a particular day, analogue days with similar circulation conditions are chosen by minimizing a distance function between the circulation field (e.g., Z500′)

170   on the target day and that on historical days within a specific calendar range centered around the target day. Second, the top N analogue patterns with the smallest distance function are linearly combined to create a "constructed analogue" pattern that resembles the circulation pattern of the target day. Finally, the N coefficients from the linear combination are applied to P' values of the N analogue days to obtain P'_{dyn}. The flow analogue method generally provides a better estimate of dynamic contribution compared to the C2007 method, as it explains a larger portion of

175   the observed P' variance. This improvement is primarily due to the flow analogue method considering the differences

among circulation patterns in individual analogue days and combining P' values from these analogue days. However, flow analogue is less effective than the C2007 method when evaluating the relationship between a specific circulation type and P'.

In this study, we propose a new method called SOM-Analogue (SOMA) that combines the advantages of both SOM (C2007) and flow analogue. SOMA aims to be capable of quantifying overall circulation contribution and the contribution of a specific circulation type to P', and also provide a more robust P'_{dyn} estimate that is less sensitive to the choice of parameters and explains a large portion of observed P' variability. The basic idea behind SOMA is to incorporate variability in P'_{dyn} for days with the same BMU node, similar to the flow analogue method, while adhering to the C2007 framework. In contrast to the flow analogue method, where analogue days are determined by minimizing the Euclidean distance of anomalous circulation patterns, in SOMA, the analogue days are directly selected from the daily samples sharing the same BMU. The detailed steps of the SOMA method are listed as follows.

1) After PCA preprocessing, the original circulation anomaly matrix $\mathbf{Y}_{Np \times Nt}$ can be written as $\mathbf{Y}_{Np \times Nt} = \mathbf{V}_{Np \times Ne} \cdot \mathbf{X}_{Nt \times Ne}^T$, where N_p is the number of grid points (61×31) multiplied by the number of circulation variables (2), N_t the number of days, and N_e the number of all PCs. By only retaining the top K PCs, $\mathbf{Y}_{Np \times Nt} \approx \mathbf{V}_{Np \times K} \cdot \mathbf{X}_{Nt \times K}^T$.

2) The PC matrix $\mathbf{X}_{Nt \times K}$ is used as input to train a SOM. For each daily sample $\mathbf{x}_t$ (1×K) at time t, we can find its corresponding BMU, i.e., BMU($\mathbf{x}_t$) = $\mathbf{B}_i$, where $\mathbf{B}_i$ is one of the SOM nodes, and i (i = 1, 2, 3, …, N) can be determined by minimizing the Euclidean distance between $\mathbf{x}_t$ and $\mathbf{B}_i$. The circulation pattern for node i can be then recovered as $\mathbf{V}_{Np \times K} \cdot \mathbf{B}_i^T$.

3) For any day t_0, assuming its BMU is node i, we find all days t_j (j = 1, 2, …, M) that have this node i as their BMU and are within the 91-day calendar window centered on the day t0 but not in the same year as t0, i.e., BMU($\mathbf{x}_{tj}$)=BMU($\mathbf{x}_{t0}$), |DOY(t_j) – DOY(t_0)| ≤ 45 d, Year(t_j)≠Year(t_0).

4) Solve the regression problem: $\mathbf{P}_{1 \times M} = \mathbf{U}_{1 \times K} \cdot \mathbf{X}_{M \times K}^T$, where $\mathbf{P}_{1 \times M}$ is the precipitation vectors for days t_j (j = 1, 2, …, M) from the previous step, $\mathbf{X}_{M \times K}$ is input PC samples for these M days. The regression coefficient vector $\mathbf{U}_{1 \times K}$ is then used to calculate the dynamic precipitation anomaly for the day t_0, $P'_{dyn,t0} = \mathbf{U}_{1 \times K} \cdot \mathbf{x}_{t0}^T$.

5) Repeat steps 3) and 4) for all days until all P'_{dyn} are calculated.

To account for the sampling uncertainty, we apply a bootstrap technique in step 3) where we create multiple data sets of $\mathbf{X}_{M \times K}$ by randomly sampling $\mathbf{x}_{tj}$ with replacement. After bootstrapping and repeating step d) for 1000 times, the 1000 calculated $P'_{dyn,t0}$ are then averaged as the final result.

This SOMA method described above employs the idea of constructed flow analogue that the contribution of circulation to precipitation anomaly is a linear combination of precipitation anomaly in its analogue days, where the coefficients are determined by the linear dependency of current circulation pattern on the analogue circulation patterns. This omits the possible thermodynamic influences in the precipitation anomaly in these analogue days. Therefore, the calculated dynamic component, i.e., a linear combination of the analogue day precipitation anomalies, can still retain a thermodynamic residual. Here, we assume that for each group of similar circulation pattern (same SOM node) within a certain calendar range (91 days), P'_{dyn} of any day is equal to a linear combination of P'_{dyn} of other days in the same group, which does not contain thermodynamic component of P' as in the analogue approach. As each circulation pattern is linearly dependent on other circulation patterns in the same group, P'_{dyn} should have the same linear

dependency. Since we use PCA approximation for the circulation patterns ($Y_{Np \times M} \approx V_{Np \times K} \cdot X_{M \times K}^T$), the underlying assumption is that P'_{dyn} has the same PC components as the circulation ($P_{1 \times M} \approx U_{1 \times K} \cdot X_{M \times K}^T$). Thus, calculation of P'_{dyn} becomes a regression problem that can be solved by the step 4) above.

3 Result

3.1 Atmospheric circulation pattern clustering and link to precipitation

After the 7×4 SOM for Z500′ and IVT′ is trained and each daily sample is assigned to its BMU node, circulation patterns with the same BMU node are averaged as the general representation of circulation condition for the particular node. The composite circulation anomaly patterns for all SOM nodes are shown in Fig. 2. Similar to our earlier study (Zhuang et al., 2020), the SOM map shows a continuum of anomalous circulation and moisture transport patterns over the CONUS. Regions with large Z500′ gradients often correspond to large IVT′ due to the geostrophic balance relationship. For example, when an anomalous geopotential low is centered over the western or central US and a geopotential high over the eastern or southeastern US (e.g., nodes A1, B1, C1, C2, D1, D2, and D3), enhanced moisture transport from the Gulf of Mexico represented by the large positive IVT′ is often observed in-between the geopotential low and high with elevated geopotential gradient.

As the SOM is trained with daily samples of all seasons and considering the potential seasonal variation of occurrence frequency and circulation-precipitation relationship, we calculate the frequency and average P' for each SOM node during every 91-day calendar window during all years. The resulted seasonal variations of node frequency and mean P' are shown in Fig. 3 and Fig. 4, respectively. In Fig. 3, some nodes exhibit very clear seasonal variation with the range of frequency being as large as 4%; they either peak in cold seasons, such as C1 and D1, with the anomalous geopotential high centered more to the southeastern US and strong moisture transport to the SGP, or peak in the warm seasons, such as C4 and D4 where the high is centered more to the northeastern US so the moisture transport is weaker and more towards the north. Some other nodes show relatively stable frequency throughout the year, with a range of less than 1%, such as nodes C6, C7, and D7 where the CONUS is mostly dominated by an extensive geopotential high.

Similarly for precipitation, it also shows apparent seasonal variations for certain nodes (Fig. 4). For example, node D1, located at the lower-left corner of the SOM, brings the strongest positive IVT′ from the Gulf of Mexico and the Gulf of California of all nodes, and it is one of the major wet nodes related to positive P' in all three regions during the cold season. However, during the warm season, node D1 is more of a neutral or weakly dry node as it is linked to a small negative P' in the SGP; for the NGP, this node is still a wet node and the average P' is larger than that during the cold season. This can in part be explained by the seasonal difference in precipitation mechanisms. In the warm season, precipitation is mostly convective-driven so large-scale vertical air motion of some circulation patterns have fewer impacts on precipitation; on the other hand, the composite CAPE′ and CINi′ map for node D1 (Fig. 5) shows relatively smaller CAPE′ and a more stable lower troposphere (negative CINi′) in the warm season (May to July), as opposed to D1 in the cold season (November to January), suppressing convective initiation and development thus limiting precipitation regardless of the strong moisture transport. Similar situations occur to many other nodes as well

with either opposite signs of mean P' in different seasons or same sign but with clear seasonal variations. Overall, these seasonalities of circulation-precipitation relationship can be attributed to factors controlling the types and mechanisms of precipitation that can vary seasonally, such as atmospheric stability and soil moisture feedback, or slight sampling bias in different seasons as shown by the contrast between composite circulation maps for the same node in different seasons (Fig. 5).

3.2 Dynamic and thermodynamic contributions to precipitation

The above analyses show that strong seasonal variations could exist for either frequency or mean P' in certain nodes due to different types of precipitation and factors other than large-scale circulation and moisture transport that contribute to precipitation. Therefore, assuming node-mean P' as dynamic components calculated using the C2007 method may result in an incorrect representation of dynamic contribution and underestimation of its variability.

The second part of our analysis is to employ the SOMA method described in the method section to estimate the contribution of dynamics and thermodynamics to P'. We decompose the daily average P' of certain regions (SGP, NGP, and SW) into the sum of a dynamic component P'_{dyn} which is explained by the mid-tropospheric circulation and moisture transport, and a thermodynamic component P'_{the} which ideally should be independent of circulation condition and related to thermodynamic processes such as land surface feedbacks. Further analysis shows that composite seasonal cycles of P'_{dyn} for different nodes are similar to that of P' (Fig. 4) but with narrower IQR (not shown). In contrast, P'_{the} does not show a clear season cycle for any node (not shown). This indicates the majority of precipitation variation at daily to synoptic scale can be mainly explained by dynamics, and thermodynamics does not have a preference for certain nodes in any season. The P'_{dyn} calculated by our SOM-based method overall is highly correlated to P' in all seasons, indicating circulation and moisture transport conditions can explain a large portion of precipitation variability.

Fig. 6A shows the percentage of the variance of P' explained by the P'_{dyn} (R_{dyn}^2). NGP, which is located more to the north and more susceptible to frontal weather systems has the largest mean R_{dyn}^2 of 60.5% for all year round, while SW and SGP have slightly smaller values of 56.3% and 53.6%, respectively. These three regions also show very clear seasonal variations of R_{dyn}^2 as well: regions located more to the south like the SGP and SW, show a maximum of ~60% and ~70% in winter (December to January) when precipitation is more affected by frontal systems and a minimum of ~45% and ~40% in summer (July to August) when precipitation is mostly convectively driven and surface thermodynamic has more influences. On the other hand, the more northern region NGP shows continuous higher in the warm season (March to October); its seasonal variation of R_{dyn}^2 shows two local minima, one in August (~55%) and the other in January (~50%), and two local maxima, one in April-May (~65%) and the other in October-November (~64%).

In addition to daily precipitation variability, we fit a simple linear regression model $P'_{dyn} = \beta P'$ for each 91-day calendar window in each region to estimate the relative percentage dynamic contribution (β) to intensity of the precipitation anomaly. Fig. 6B shows the seasonal variation of β for all samples at daily scale for each region. Overall, the percentage dynamic contributions in the SGP and SW show a similar seasonal cycle as the R_{dyn}^2, with the highest β

(~69% and ~73%) in the cold season (December to January) and the lowest (~56% and ~50%) in the warm season (May to August), while the NGP has a mean β of ~68% with a smaller range of seasonal variation (~65% to ~75%).

285 Fig. 7 further shows the historical evolution of 12-month moving average P' and its dynamic and thermodynamic components from 1950 to 2021 to demonstrate how dynamics and thermodynamics contribute to the longer term variability of precipitation. Overall, P'_{dyn} matches better with P' than P'_{the} does for all three regions, even for some P' extremes during major drought and flooding events. Percentage variance explained by the dynamic component is 87.3%, 82.1%, and 82.8% for SGP, NGP, and SW, respectively, which are considerably higher than that explained by

290 the thermodynamics (62.6%, 77.2%, and 65.5%). This suggests atmospheric circulation and moisture transport are the main controls for precipitation variations at interannual scale as well.

To further demonstrate what type of atmospheric circulation patterns are most related to regionally dry and wet anomalies, Fig. 8 ranks the nodes according to their mean seasonally cumulative P'_{dyn} and P'_{the} during four seasons, including January to March (JFM), April to June (AMJ), July to September (JAS), and October to December (OND).

295 As these seasonal contributions are averaged over all years, many nodes show clear tendency to be dynamically related to either dry or wet anomaly during a particular season in a region, but almost all of them have negligible thermodynamic component. Consistently through all three regions, the top four nodes contribute most to dry anomalies in the cold season (JFM and OND) are A7, B7, C7, and D7, all located in the right side of the SOM map, featuring either a west high-east low or high-dominant geopotential pattern over the CONUS with reduced IVT' in both SGP

300 and SW. On the other hand, for the wet anomalies, top contributing nodes are mostly located in the left or bottom side of the SOM map, featuring a west low-east high geopotential pattern favoring increased IVT'.

In the warm season (AMJ and JAS), top dry and wet nodes all change a bit for the three regions. For example, for the SGP, besides the high-dominant pattern D6 and D7, a few west low-east high patterns (C3, D2, D3) with increased IVT' also contribute considerably to P'_{dyn} due the increased lower atmospheric stability related (CIN') related to them.

305 For the SW, A1 becomes the top contributing node in its monsoon season due to the weak geopotential gradient there and the strong geopotential high in the west coast, all of which reducing the main moisture source, including that from the Gulf of Mexico and Gulf of California.

3.3 Long-term changes of precipitation

As the results from the previous section already suggest that dynamic factors (circulation and moisture transport) can

310 explain the majority of variance of precipitation anomalies from daily to interannual variability, our next question to investigate is whether precipitation show long term changes and how does these changes can be explained by the circulation changes, which is mainly related to internal variability of the atmosphere and oceanic forcings. The PDO has been demonstrated as a main oceanic forcing that controls the multi-decadal variability of precipitation over the North America, as PDO can generate atmospheric circulation patterns that favor dry or wet condition (Lehner et al.,

315 2018). Our period of analysis, i.e., 1950-2021, mainly encompasses three periods with shifting PDO phases, including P1: 1950-1976 (mostly negative), P2: 1977-1998 (mostly positive), and P3: 1999-2021 (mostly negative).

Fig. 9 (1st column) shows the period mean P' for different seasons and regions and contrasts them in three periods with different PDO phases. We can see that, overall, for all season, all three regions all show very significant increase

of P' from P1 to P2, and then a decrease from P2 to P3. These increase and decrease are both due to changes in more
than one season, though it is not consistent through all seasons: for example, SGP shows negligible changes in JAS
and NGP shows increase of P' instead of decrease from P2 to P3. The dynamic component P'_{dyn} (2nd column in Fig.
9), though generally has a smaller amplitude of anomaly, captures the multi-decadal changes of the P' in the three
periods (from 14% to 82% for all seasons, Table 2), especially for the SW (75% and 82% of the changes in P1 − P2
and P2 − P3).

To further determine how much of the dynamic contribution to the multi-decadal changes of P' can be linked to PDO
changes, we first determine nodes that are potentially related to PDO phase change using a Monte-Carlo test with the
following steps: a) for node k in month m, calculate the difference between the node frequency with positive PDO
phase (monthly PDO index > 0.5) and that with negative phase (monthly PDO index < -0.5) for all years, i.e., $\Delta f_{k,m}$;
b) randomly shuffle the sequence of years for the PDO index data and recalculate the frequency difference $\Delta f_{k,m}*$; c)
repeat step b) for many times (1000 here), if $\Delta f_{k,m}$ is larger or smaller than 90% of all $\Delta f_{k,m}*$, then node k is considered
a PDO related node in month m. The resulted nodes statistically related to PDO in each month are shown in Fig. 10.
There are considerably more PDO-related nodes in the cold season from October to March (~10.3 nodes/month) than
in the warm season from April to September (~4.7 nodes/month), consistent with previous studies that oceanic forcing
has more influence on North America precipitation variability in the cold season than in the warm season due to the
more atmospheric wave train activities excited by Pacific SST anomalies (Ciancarelli et al., 2014; Ropelewski and
Halpert, 1986).

Once the PDO-related nodes are identified, we calculate the dynamic contribution to the period mean P' and
accumulate them only for days with these PDO-related nodes and the result is shown in Fig. 9 (3rd column). We can
see that although the PDO-related nodes we identified only constitute a small fraction of all nodes (~36.9% and
~16.7% in the warm and cold season, respectively), PDO-related P'_{dyn} shows very similar multi-decadal changes as
the total P'_{dyn}. Table 1 summarizes the total and PDO-related dynamic contribution to the multi-decadal changes of
P'. The dynamic contributions are highest for the SW (74.9% to 81.9%), with only less than 1/3 are PDO-related
(24.9% to 21.1%). For the other two regions (SGP and NGP) with smaller dynamic contribution, PDO-related P'_{dyn}
also explain a relatively smaller portion of the total P' change (15% to 18%), except for P2→P3 change in the NGP
(56%), where the absolute P' change is smallest.

In addition to the change of mean P', change of P' extremes are also of interest because these extremes are more
impactful. Fig. 11 shows the probability density plot of percentile precipitation anomalies for P' and P'_{dyn} in the three
periods. During P1→P2, all three regions show a reduced probability of dry extremes and increased probability of wet
extremes. For the SGP and NGP, this decrease of dry extremes was more prominent in the warm season than in the
cold season; the increase of wet extremes, though also varies seasonally, shows larger change than dry extremes and
can be found in all seasons. In the second period change P2→P3, as the PDO shifted back to the negative phase, all
three regions show increase of dry extremes and decrease of wet extremes, but it did not recover to the level as in P1,
i.e., less dry extremes and more wet extremes than in P1. This is potentially because anthropogenic warming has
increased the moisture in the atmosphere thus the recent P3 period favored wetter condition and wet extremes more
than the P1 period with the same negative PDO phase.

The dynamic components P'_{dyn} have relatively flat curves at the drier side of the distribution (<10th percentile; defined as dry extremes), inconsistent with the P' distribution, as dry extremes tend to be accompanied with stronger thermodynamic feedback; on the wetter side of the distribution (>90th percentile; defined as wet extremes), higher consistency between P' and P'_{dyn} can be observed. Table 2 summarizes these observed changes of dry and wet extreme

360   days and the corresponding total and PDO-related dynamic contribution. For the SGP and NGP, there is a ~5 d/yr decrease of dry extremes and ~10 d/yr increase of wet extremes during the earlier PDO shift (P1→P2, negative to positive); dynamic contribution accounts for over 90% and PDO-related dynamics contributes ~25% to the change in the SGP, while the percentages are much smaller for the NGP. However, during the recent PDO shift (P2→P3, positive to negative), the change of both dry and wet extremes in the SGP and NGP have considerably smaller amplitude

365   compared to that during P1→P2, which could be related to the anthropogenic warming induced increase in atmospheric moisture. SW has much larger change of extremes (-24 d/yr and +17 d/yr for dry and wet in P1→P2, +5 d/yr and -14 d/yr in P2→P3) compared to other two regions during P1→P2, and dynamics overall explains a significant portion of the changes, though only less than half of the dynamic contribution can be potentially related to PDO phase shift, indicating the atmospheric internal variability could play an important role in the precipitation extreme changes

370   as well.

4 Summary and Discussion

SOM has been demonstrated as an effective way of identifying and visualizing large-scale circulation patterns related to various surface anomalies, such as precipitation and temperature (Liu and Weisberg, 2011). However, SOM-based approach to quantify the contribution of anomalous circulation pattern on surface anomalies is not as reliable. On the

375   other hand, flow analogue (including many of its variants) or the so-called dynamical adjustment technique has long been used as an important empirical approach to acquire or remove circulation anomaly variability, though it is not an effective way in terms of demonstrating what types of circulation is responsible for specific surface anomalies or quantifying the contribution from a specific group of circulation. Building upon the previous studies related to these two methods, we develop a dynamic/thermodynamic contribution partition approach based on both the two above-

380   mentioned methods and use it to investigate the large-scale atmospheric circulation and moisture transport pattern related to the dry and wet precipitation anomalies over the U.S. Great Plains (SGP and NGP) and the Southwest (SW), as well as the dynamic and thermodynamic contribution to these anomalies, in terms of their daily to interannual variability and long term multi-decadal changes.

First part of our results is a traditional SOM clustering analysis based on the large-scale atmospheric circulation

385   anomaly pattern, including mid-tropospheric geopotential height (Z500′) and moisture transport (IVT′). We showed that many of these SOM nodes, i.e., types of circulation, have distinctive seasonal variations in terms of their frequencies of occurrence and regional precipitation anomalies related to them. This change of the circulation-precipitation relationship is in part due to the seasonal difference in the main mechanisms producing the precipitation. For example, warm season precipitation is mainly convectively driven so it is more related to convective energy and

390   atmospheric stability, therefore nodes favoring wet condition in the cold season which feature intense moisture transport (e.g., node D1, Fig. 4) could be linked to dry or neutral precipitation anomalies due to the less desirable

convective statistics related to the same circulation condition. We then went on to develop a SOM-Analogue approach and use the trained SOM to estimate the dynamic and thermodynamic contribution to precipitation anomalies over the SGP, NGP, and SW regions. Overall, dynamics (circulation condition represented by Z500 and IVT) explains the

395 majority of the variability and amplitude of P', with higher explained ratio in the cold season than in the warm season, and higher over the northern region (NGP) than the southern regions (SGP and SW). We also showed that the main nodes responsible for dry or wet anomalies could differ largely depending on seasons and regions of interest. The last part of the study further uses the partition results to estimate how much circulation can explain the multi-decadal shift of dry and wet mean P' and extremes between 1950-1976, 1977-1998, and 1999-2021, and how much the PDO-related

400 circulation can explain them given the overall distinctive PDO phase in each of the three periods. Our result suggests circulation explains the shift of mean P' best in the SW (75-82%), with the PDO-related circulation occupying a large portion (21-25%); while circulation may account for a greater proportion of variability and amplitude in daily P' over the NGP compared to the other two more southern regions, it contributes less to the multi-decadal change in mean P'. The result is somewhat similar for the change of wet extreme days between the periods, with circulation and PDO-

405 related circulation explaining a higher portion over the SW than over the SGP and NGP; circulation contribution drops significantly for change of dry extreme days than that of wet extreme days, indicating thermodynamic factors such as land surface feedbacks and anthropogenic warming may play a more important role in the increase of dry extremes during the past decades.

This work demonstrates the effectiveness of the proposed SOM-Analogue in estimating circulation contribution to

410 precipitation anomalies. This approach has the advantages of the C2007 SOM-based method, i.e., easy visualization of the circulation-surface anomaly relationship and quantification of contribution from different types of circulation, yet is less sensitive to the choice of node numbers. It also has a comparable performance as the constructed flow analogue method (Zhuang et al., 2021b) in terms of R_{dyn}^2 (not shown), but P'_{dyn} calculated with SOM-Analogue does not contain a thermodynamic residual as that in the analogue method (linear combination of P'_{the} in analogue days).

415 However, this is still a statistical method with certain assumptions, so limitations still exist. For example, it could become less reliable when fewer samples are presented; both analogue and SOM-Analogue approaches all assume a constant circulation-surface anomaly relationship which might not hold true in a changing climate. In addition, our result might overestimate the PDO-related circulation contribution to P' as the frequency changes of PDO-related node could be due to both PDO phase changes, atmospheric internal variability, as well as anthropogenic warming induced

420 change in circulation (Horton et al., 2015).

Competing Interests

The contact author has declared that none of the authors has any competing interests.

Acknowledgement

This study was supported by funding from the National Oceanic and Atmospheric Administration-Climate Program

425 Office (NOAA-CPO), Modeling, Analysis, Predictions, and Projections (MAPP) Program (NA20OAR4310426).

References

Cassano, J. J., Uotila, P., Lynch, A. H., and Cassano, E. N.: Predicted changes in synoptic forcing of net precipitation in large Arctic river basins during the 21st century, J Geophys Res-Biogeo, 112, Artn G04s49, 10.1029/2006jg000332, 2007.

430 Christidis, N. and Stott, P. A.: Changes in the geopotential height at 500hPa under the influence of external climatic forcings, Geophys Res Lett, 42, 10798-10806, 10.1002/2015gl066669, 2015.

Ciancarelli, B., Castro, C. L., Woodhouse, C., Dominguez, F., Chang, H. I., Carrillo, C., and Griffin, D.: Dominant patterns of US warm season precipitation variability in a fine resolution observational record, with focus on the southwest, Int J Climatol, 34, 687-707, 10.1002/joc.3716, 2014.

435 Deser, C., Terray, L., and Phillips, A. S.: Forced and Internal Components of Winter Air Temperature Trends over North America during the past 50 Years: Mechanisms and Implications, J Climate, 29, 2237-2258, 10.1175/Jcli-D-15-0304.1, 2016.

Elias, E., Rango, A., Smith, R., Maxwell, C., Steele, C., and Havstad, K.: Climate Change, Agriculture and Water Resources in the Southwestern United States, J Contemp Wat Res Ed, 158, 46-61, 10.1111/j.1936-
440 704X.2016.03218.x, 2016.

Hersbach, H., Bell, B., Berrisford, P., Hirahara, S., Horanyi, A., Munoz-Sabater, J., Nicolas, J., Peubey, C., Radu, R., Schepers, D., Simmons, A., Soci, C., Abdalla, S., Abellan, X., Balsamo, G., Bechtold, P., Biavati, G., Bidlot, J., Bonavita, M., De Chiara, G., Dahlgren, P., Dee, D., Diamantakis, M., Dragani, R., Flemming, J., Forbes, R., Fuentes, M., Geer, A., Haimberger, L., Healy, S., Hogan, R. J., Holm, E., Janiskova, M., Keeley, S., Laloyaux, P., Lopez, P.,
445 Lupu, C., Radnoti, G., de Rosnay, P., Rozum, I., Vamborg, F., Villaume, S., and Thepaut, J. N.: The ERA5 global reanalysis, Q J Roy Meteor Soc, 146, 1999-2049, 10.1002/qj.3803, 2020.

Hoerling, M., Eischeid, J., Kumar, A., Leung, R., Mariotti, A., Mo, K., Schubert, S., and Seager, R.: Causes and Predictability of the 2012 Great Plains Drought, B Am Meteorol Soc, 95, 269-282, 10.1175/Bams-D-13-00055.1, 2014.

450 Horton, D. E., Johnson, N. C., Singh, D., Swain, D. L., Rajaratnam, B., and Diffenbaugh, N. S.: Contribution of changes in atmospheric circulation patterns to extreme temperature trends, Nature, 522, 465-+, 10.1038/nature14550, 2015.

Hu, Q. and Feng, S.: Variation of the North American summer monsoon regimes and the Atlantic multidecadal oscillation, J Climate, 21, 2371-2383, 10.1175/2007jcli2005.1, 2008.

455 Hu, Z. Z. and Huang, B. H.: Interferential Impact of ENSO and PDO on Dry and Wet Conditions in the US Great Plains, J Climate, 22, 6047-6065, 10.1175/2009jcli2798.1, 2009.

Jezequel, A., Yiou, P., and Radanovics, S.: Role of circulation in European heatwaves using flow analogues, Clim Dynam, 50, 1145-1159, 10.1007/s00382-017-3667-0, 2018.

Kaski, S., and Lagus, K.: Comparing Self-Organizing Maps, In Proceedings of International Conference on Artificial
460 Neural Networks (ICANN), 1996.

Kirchmeier-Young, M. C. and Zhang, X. B.: Human influence has intensified extreme precipitation in North America, P Natl Acad Sci USA, 117, 13308-13313, 10.1073/pnas.1921628117, 2020.

Kohonen, T.: The Self-Organizing Map, P Ieee, 78, 1464-1480, 10.1109/5.58325, 1990.

Lehner, F., Deser, C., Simpson, I. R., and Terray, L.: Attributing the US Southwest's Recent Shift Into Drier
465 Conditions, Geophys Res Lett, 45, 6251-6261, 10.1029/2018gl078312, 2018.

Liu, Y. G. and Weisberg, R. H.: A Review of Self-Organizing Map Applications in Meteorology and Oceanography, Self Organizing Maps - Applications and Novel Algorithm Design, 253-272, Book_Doi 10.5772/566, 2011.

Mankin, J. S., Simpson, I., Hoell, A., Fu, R., Lisonbee, J., Sheffield, A., and Barrie, D.: NOAA Drought Task Force Report on the 2020–2021 Southwestern U.S. Drought, NOAA Drought Task Force, MAPP, and NIDIS, 2021.

470 McKinnon, K. A. and Deser, C.: The Inherent Uncertainty of Precipitation Variability, Trends, and Extremes due to Internal Variability, with Implications for Western US Water Resources, J Climate, 34, 9605-9622, 10.1175/Jcli-D-21-0251.1, 2021.

Myoung, B. and Nielsen-Gammon, J. W.: The Convective Instability Pathway to Warm Season Drought in Texas. Part I: The Role of Convective Inhibition and Its Modulation by Soil Moisture, J Climate, 23, 4461-4473,
475 10.1175/2010jcli2946.1, 2010.

NOAA National Centers for Environmental Information (NCEI): U.S. Billion-Dollar Weather and Climate Disasters, https://www.ncei.noaa.gov/access/billions/, Doi 10.25921/stkw-7w73, 2023.

Parton, W. J., Gutmann, M. P., Merchant, E. R., Hartman, M. D., Adler, P. R., McNeal, F. M., and Lutz, S. M.: Measuring and mitigating agricultural greenhouse gas production in the US Great Plains, 1870-2000, P Natl Acad Sci
480 USA, 112, E4681-E4688, 10.1073/pnas.1416499112, 2015.

Pu, B., Dickinson, R. E., and Fu, R.: Dynamical connection between Great Plains low-level winds and variability of central Gulf States precipitation, J Geophys Res-Atmos, 121, 3421-3434, 10.1002/2015jd024045, 2016.

Reusch, D. B., Alley, R. B., and Hewitson, B. C.: Relative Performance of Self-Organizing Maps and Principal Component Analysis in Pattern Extraction from Synthetic Climatological Data, Polar Geogr, 29, 188-212, 10.1080/789610199, 2005.

Ropelewski, C. F. and Halpert, M. S.: North-American Precipitation and Temperature Patterns Associated with the Elnino Southern Oscillation (Enso), Mon Weather Rev, 114, 2352-2362, Doi 10.1175/1520-0493(1986)114<2352:Napatp>2.0.Co;2, 1986.

Seager, R., Goddard, L., Nakamura, J., Henderson, N., and Lee, D. E.: Dynamical Causes of the 2010/11 Texas-Northern Mexico Drought*, J Hydrometeorol, 15, 39-68, 10.1175/Jhm-D-13-024.1, 2014.

Siler, N., Proistosescu, C., and Po-Chedley, S.: Natural Variability Has Slowed the Decline in Western US Snowpack Since the 1980s, Geophys Res Lett, 46, 346-355, 10.1029/2018gl081080, 2019.

Swales, D., Alexander, M., and Hughes, M.: Examining moisture pathways and extreme precipitation in the US Intermountain West using self-organizing maps, Geophys Res Lett, 43, 1727-1735, 10.1002/2015gl067478, 2016.

Vatanen, T., Osmala, M., Raiko, T., Lagus, K., Sysi-Aho, M., Oresic, M., Honkela, T., and Landesmaki, H.: Self-organization and missing values in SOM and GTM, Neurocomputing, 147, 60-70, 10.1016/j.neucom.2014.02.061, 2015.

Yiou, P., Vautard, R., Naveau, P., and Cassou, C.: Inconsistency between atmospheric dynamics and temperatures during the exceptional 2006/2007 fall/winter and recent warming in Europe, Geophys Res Lett, 34, Artn L21808, 10.1029/2007gl031981, 2007.

Zhang, Y., Wallace, J. M., and Battisti, D. S.: ENSO-like interdecadal variability: 1900-93, J Climate, 10, 1004-1020, Doi 10.1175/1520-0442(1997)010<1004:Eliv>2.0.Co;2, 1997.

Zhuang, Y. Z., Erfanian, A., and Fu, R.: Dryness over the US Southwest, a Springboard for Cold Season Pacific SST to Influence Warm Season Drought over the US Great Plains, J Hydrometeorol, 22, 63-76, 10.1175/Jhm-D-20-0029.1, 2021a.

Zhuang, Y. Z., Fu, R., and Wang, H. Q.: Large-Scale Atmospheric Circulation Patterns Associated With US Great Plains Warm Season Droughts Revealed by Self-Organizing Maps, J Geophys Res-Atmos, 125, ARTN e2019JD031460, 10.1029/2019JD031460, 2020.

Zhuang, Y. Z., Fu, R., Santer, B. D., Dickinson, R. E., and Hall, A.: Quantifying contributions of natural variability and anthropogenic forcings on increased fire weather risk over the western United States, P Natl Acad Sci USA, 118, ARTN e2111875118, 10.1073/pnas.2111875118, 2021b.

Table 1: Long-term mean precipitation anomaly changes across three periods with shifting PDO phases (P1: 1950-1976, PDO-; P2: 1977-1998, PDO+; P3: 1999-2021, PDO-) and the total and PDO-related dynamic contribution.

Region	Observed change (mm/d)		Dynamic contribution (%)			
			Total		PDO-related	
	P1 → P2	P2 → P3	P1 → P2	P2 → P3	P1 → P2	P2 → P3
SGP	+0.260	-0.087	62.4	28.4	18.2	17.2
NGP	+0.195	-0.043	36.4	14.4	15.2	56.0
SW	+0.211	-0.133	74.9	81.9	24.9	21.1

Table 2: Same as Table 1, but for change of extreme dry days (P' below 10th percentile) and wet days (P' above 90th percentile).

Extreme type	Region	Observed change (d/yr)		Dynamic contribution (%)			
				Total		PDO-related	
		P1 → P2	P2 → P3	P1 → P2	P2 → P3	P1 → P2	P2 → P3
Dry	SGP	-4.8	+0.1	93.1	940.6	32.4	311.6
	NGP	-6.1	-3.3	10.3	18.2	18.8	-31.1
	SW	-24.2	+5.2	23.8	50.8	8.5	11.5
Wet	SGP	+9.7	+1.2	93.8	-59.3	28.7	-8.7
	NGP	+11.0	-4.7	59.9	54.0	27.5	42.7
	SW	+16.8	-14.2	115.27	94.7	38.8	18.2
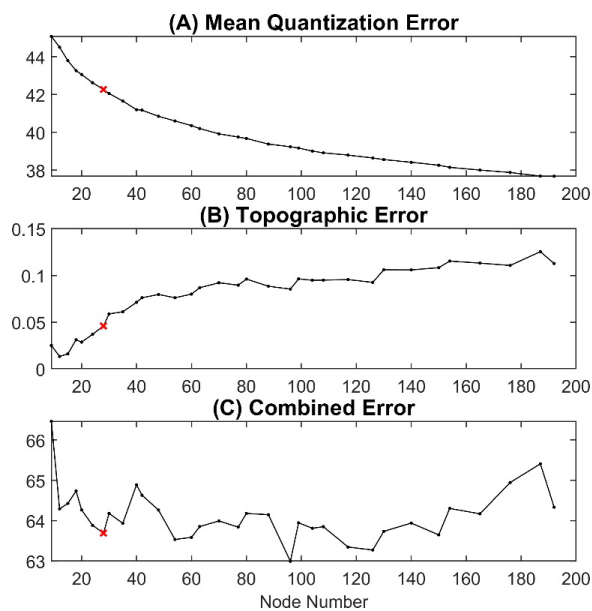
Figure 1: Quantization error (QE, A), topographic error (TE, B), and combined error (CE, C) of SOM schemes with different node numbers (N). The red cross denotes the one ($N = 28$) we select in this study.
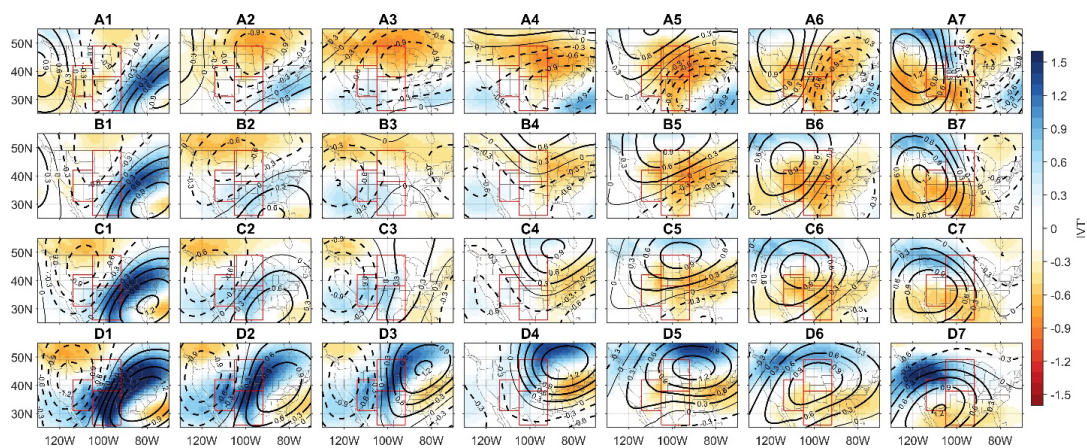
Figure 2: Composite standardized Z500′ (contours; solid and dashed lines are for positive and negative values, respectively) and standardized IVT′ (shades) for each node in the 7×4 SOM.
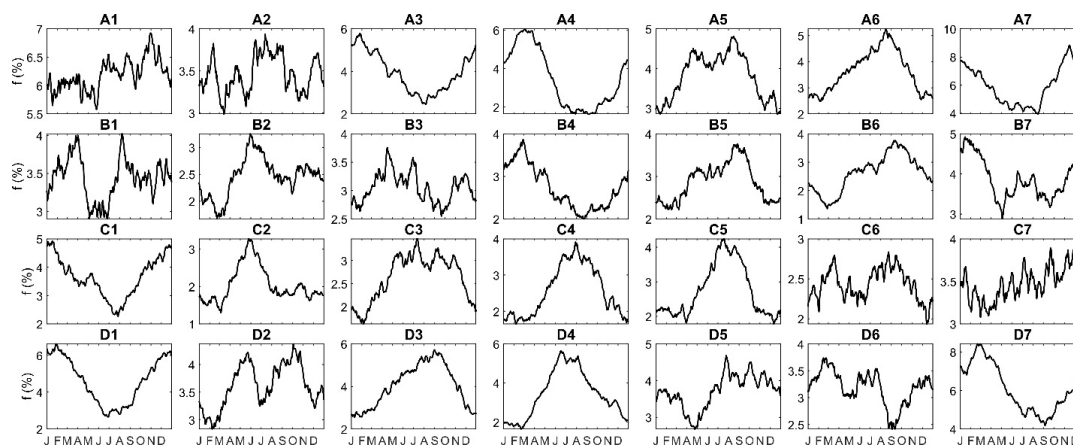
Figure 3: Seasonal variation of frequency for SOM nodes. For each node in each panel, the frequency at a certain calendar day represents the node frequency during a 91-day calendar window centered on that calendar day for all years (1950-2021).
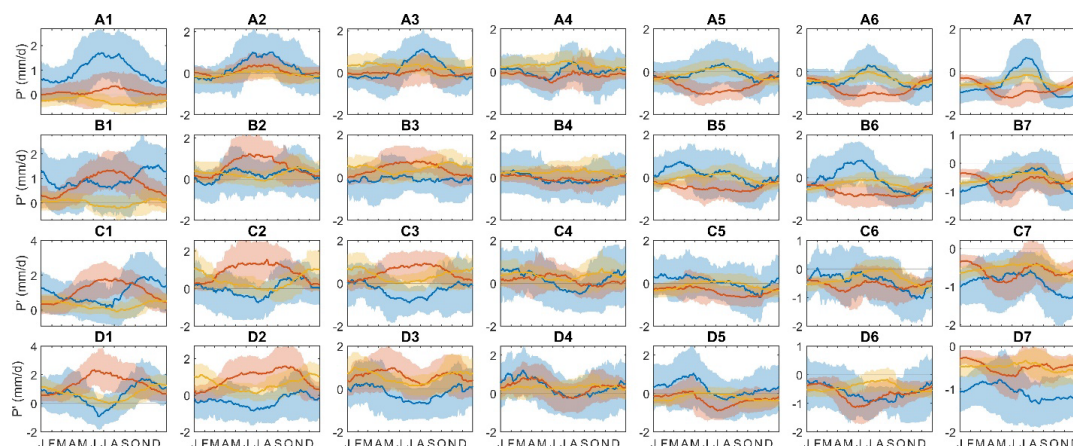
Figure 4: Seasonal variation of mean *P′* averaged over each region (blue for SGP, red for NGP, and yellow for SW) for each SOM node. For each node in each panel, the mean *P′* at a certain calendar day represents the *P′* of that node during a 91-day calendar window centered on that calendar day for all years (1950-2021). The shade represents the interquartile range of all daily *P′* used to calculate the mean.
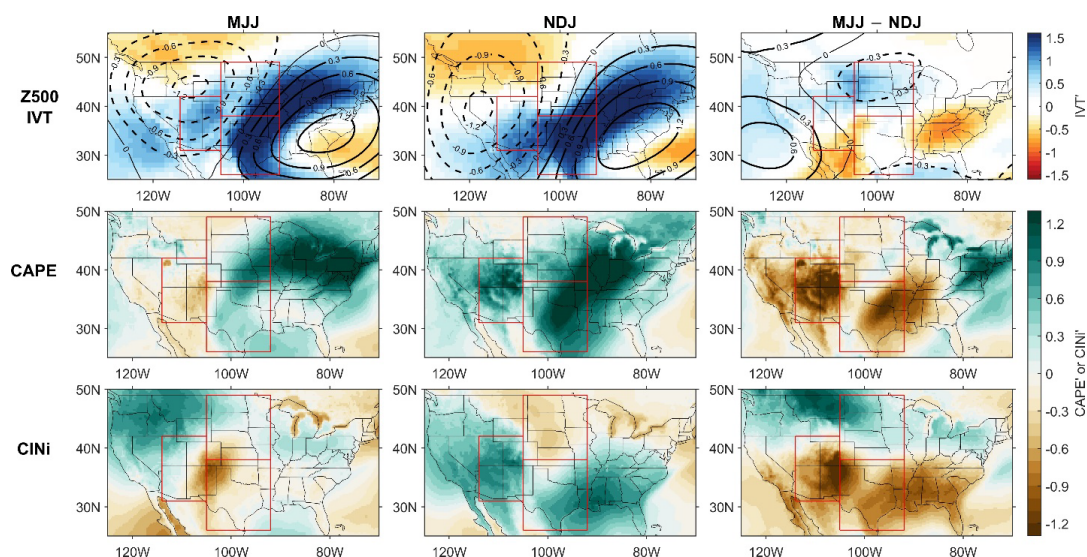
Figure 5: Composite standardized Z500′ (1st row contours), IVT′ (1st row shades), CAPE′ (2nd row), and CINi′ (3rd row)
map for node D1 during May-July (MJJ, 1st column) and November-January (NDJ, 2nd column), as well as the difference
between MJJ and NDJ (3rd column).
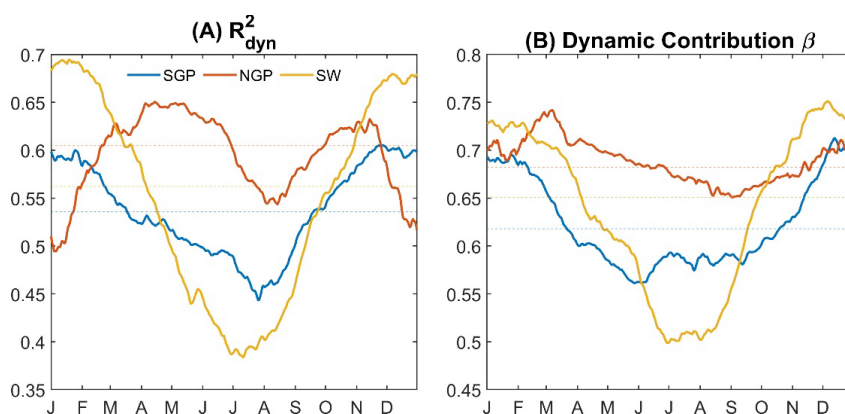
Figure 6: (A) Seasonal variation of percentage P' variance explained by P'_{dyn} (R_{dyn}^2) for the three regions; each data point
is calculated within a 91-day calendar window. Thin dashed lines represent the value for all year round. (B) Same as A, but
for seasonal variation of percentage dynamic contribution determined by fitting a simple linear regression model between
P'_{dyn} and P' during a 91-day calendar window ($P'_{dyn} = \beta P'$).
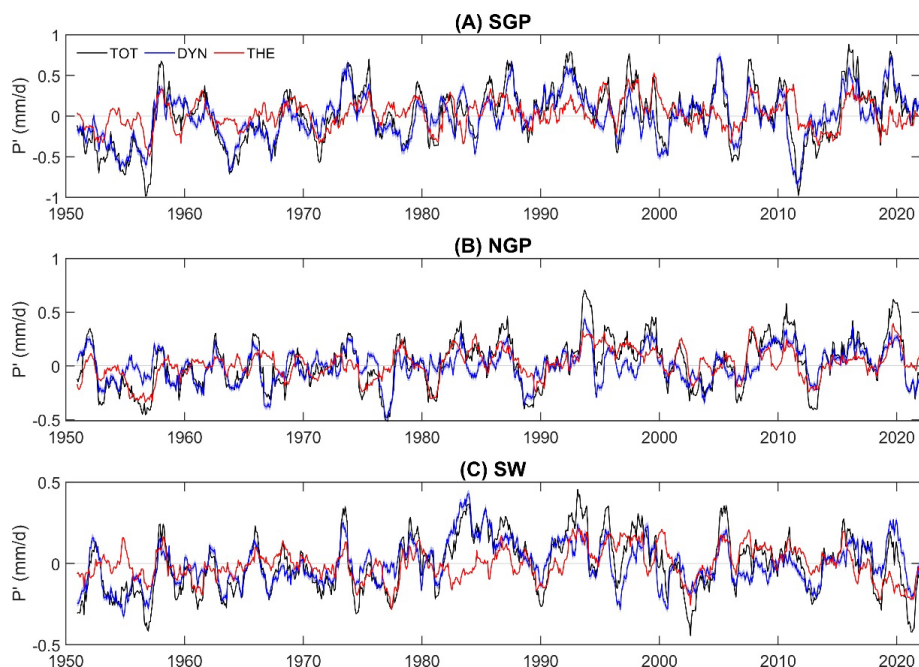
Figure 7: 12-month moving average P' (assigned to the last month of a 12-month period) for the three regions and the decomposed dynamic and thermodynamic components.
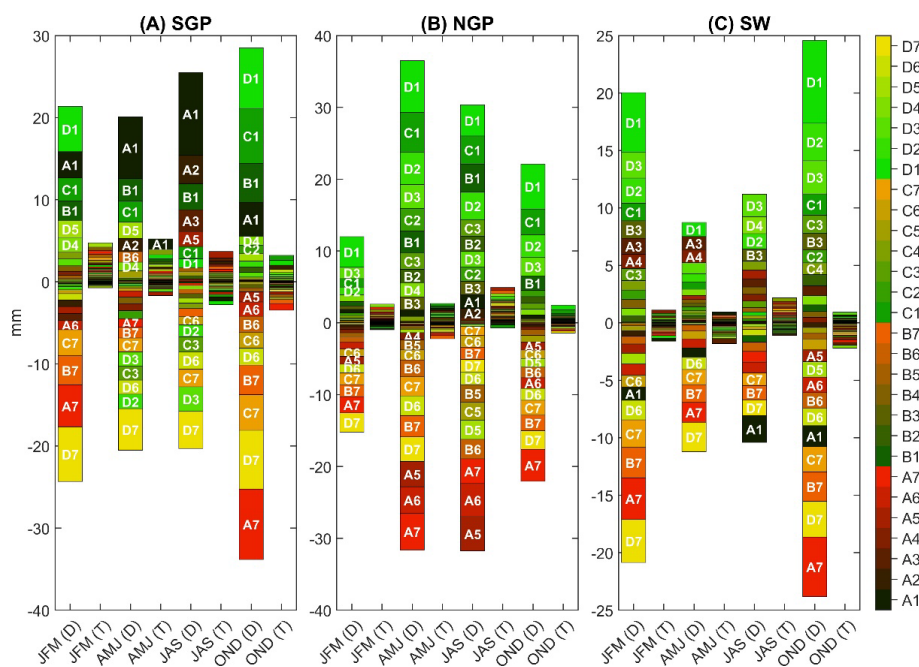
Figure 8: Average dynamic (D) and thermodynamic (T) contribution of each node in each season over the three regions.

555
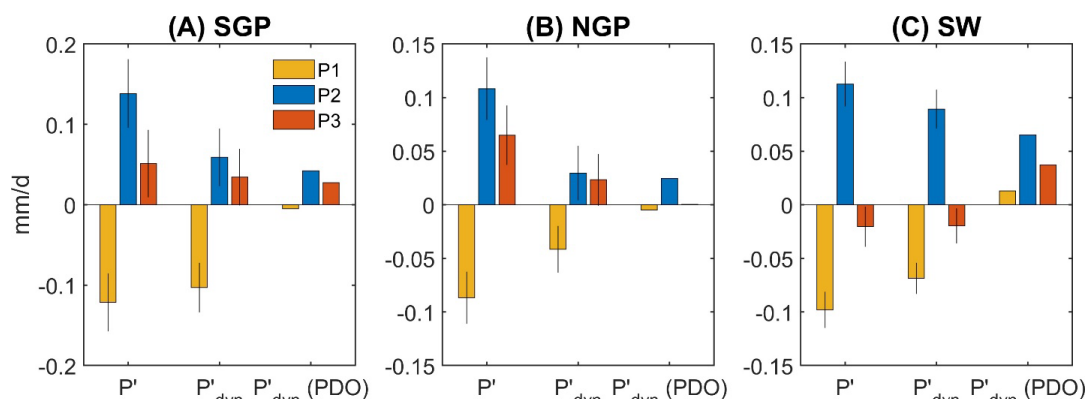
Figure 9: Mean P', P'_{dyn}, and PDO-related P'_{dyn} during three periods with shifting PDO phases (P1: 1950-1976; P2: 1977-1998; P3: 1999-2021) in the three regions: (A) SGP, (B) NGP, and (C) SW. Error bars in (A) and (B) represents the 95% confidence intervals of the mean P' and P'_{dyn}.

560
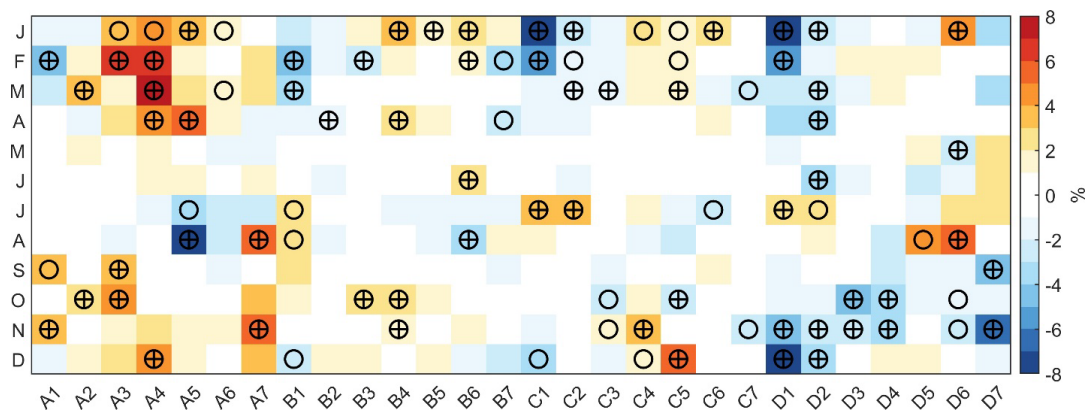
Figure 10: Node frequency difference between positive and negative PDO phases (monthly PDO index >0.5 and <-0.5) in different months. For each row or month, nodes marked with a circle (with a plus sign) indicate the frequency difference are significant positive or negative at 0.10 (0.05) level, and they can be considered PDO related nodes for that month.

565
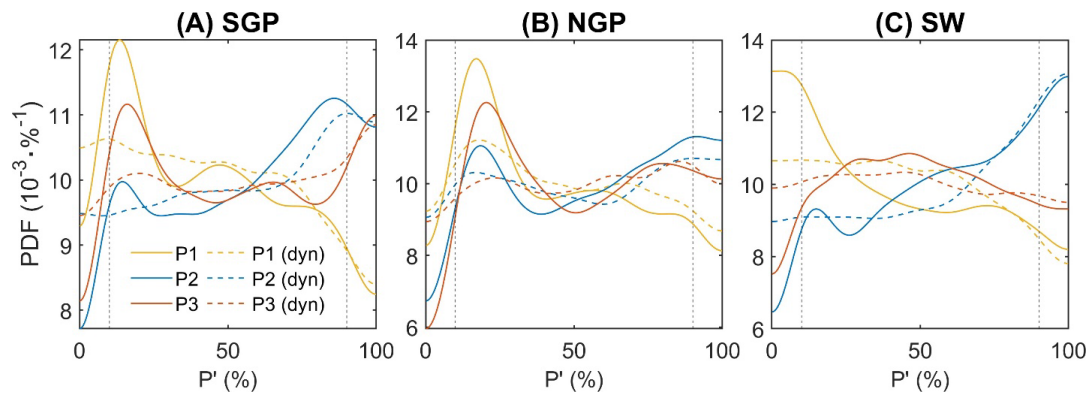
Figure 11: Kernel density plot of percentile *P′* and *P′*dyn during the three periods with shifting PDO phases (P1: 1950-1976, P2: 1977-1998, P3: 1999-2021) in three regions: (A) SGP, (B) NGP, and (C) SW. Solid and dashed lines represent percentile *P′* and *P′*dyn, respectively.

570